Current Research in Food Science 10 (2025) 100963

Contents lists available at ScienceDirect

Current Research in Food Science

journal homepage: www.sciencedirect.com/journal/current-research-in-food-science

Hyperspectral imaging for detection of macronutrients retained in glutinous rice under different drying conditions

Kabiru Ayobami Jimoh [a], Norhashila Hashim [a,b,*], Rosnah Shamsudin [c], Hasfalina Che Man [a,b], Mahirah Jahari [a,b], Puteri Nurain Megat Ahmad Azman [c], Daniel I. Onwude [d]

[a] Department of Biological and Agricultural Engineering, Faculty of Engineering, Universiti Putra Malaysia, Serdang, 43400, Selangor, Malaysia
[b] SMART Farming Technology Research Centre (SFTRC), Faculty of Engineering, Universiti Putra Malaysia, Serdang, 43400, Selangor, Malaysia
[c] Department of Process and Food Engineering, Faculty of Engineering, Universiti Putra Malaysia, Serdang, 43400, Selangor, Malaysia
[d] Empa Swiss Federal Laboratories for Material Science and Technology, ETH Zurich, Lerchenfeldstrasse 5, 9014, St. Gallen, Switzerland

ARTICLE INFO

Handling Editor: Dr. Maria Corradini

Keywords:
Dehydration
Grain processing
Food analysis
Hyperspectral imaging
Grain nutrients
Effective wavelength

ABSTRACT

This study detected the macronutrients retained in glutinous rice (GR) under different drying conditions by innovatively applying visible-near infrared hyperspectral imaging coupled with different spectra preprocessing and effective wavelength selection techniques (EWs). Subsequently, predictive models were developed based on processed spectra for the detection of the macronutrients, which include protein content (PC), moisture content (MC), fat content (FC), and ash content (AC). The result shows the raw spectra-based model had a prediction accuracy (R_p^2) of 0.6493, 0.9521, 0.4594, and 0.9773 for PC, MC, FC, and AC, respectively. Applying Savitzky Golay first derivatives (SG1D) method increases the R_p^2 value to 0.9972, 0.9970, 0.9857 and 0.9972 for PC, MC, FC, and AC, respectively. Using the variable iterative space shrinkage algorithm (VISSA) as EWs reduces the spectral bands by over 60%, and this increases the accuracy of the model (SG1D-VISSA-PLSR) to 100%. Therefore, the developed SGID-VISSA-PLSR can be used to build a smart and reliable spectral system for detecting the macronutrients in GR grains.

1. Introduction

Glutinous rice (GR) is one of Asia's most commonly cultivated and consumed rice varieties (Liu et al., 2023). The GR is known for its opaque white colour, soft texture and stickiness after cooking due to high amylopectin and low amylose content, which represent ~98% and ~2% of the total starch in the grains, respectively (Li et al., 2018). The grains have high nutritional, social and commercial value (Buresova et al., 2023). It is widely used as the raw ingredient for producing snacks, desserts, wine, crackers and flour (Ding et al., 2022). The macronutrients of the grains, including moisture, protein, fat, ash and gluten content, are some of the important quality parameters for quantifying the nutritional value of the grains (Buresova et al., 2023). According to Zhang et al. (2023), the nutritional properties of the grain play an essential role in deciding the influence and suitability of the grain processing techniques. The processing of GR begins immediately after harvesting. The phases undergone during the processing include drying, dehulling, polishing, grading, storage, and grinding. In all the processing phases, the drying process contributes tremendously to the nutrients retained in the final products (Coradi et al., 2020).

Drying of GR is an eminent pre-preprocessing stage which aids the effectiveness of the subsequent processing of the grains into a finished product (Jimoh et al., 2024a; Jimoh et al., 2023a). The primary goal of the drying process is to reduce the moisture content (MC) of the GR to a safe level for further processing (Jimoh et al., 2024b; Komolafe et al., 2025; Tu et al., 2023). During the drying process, the grains are subjected to a heated environment, leading to moisture loss due to moisture phase change and migration from the grain to the heated environment (Coradi et al., 2020; Jimoh et al., 2023b). The moisture in the grain is highly related to the quality features of the grain, such as the physical, structural, textural, and chemical properties (Dibagar et al., 2022). This infers that the drying process has a potential impact on the nutritional properties of grains. Therefore, the drying process can be controlled and enhanced by effective and rapid determination of the nutritional

* Corresponding author. Department of Biological and Agricultural Engineering, Faculty of Engineering, Universiti Putra Malaysia, Serdang, 43400, Selangor, Malaysia.
E-mail address: norhashila@upm.edu.my (N. Hashim).

https://doi.org/10.1016/j.crfs.2024.100963
Received 1 October 2024; Received in revised form 19 November 2024; Accepted 17 December 2024
Available online 21 December 2024

properties of the grain. Using the traditional methods for the determination of nutritional properties of grains is accurate and reliable when consciously carried out (Wang et al., 2022a). However, these methods are laborious, time-consuming, require high amounts of chemicals and are prone to human error, especially when dealing with large samples. Therefore, it is essential to build a reliable, low-cost, accurate, rapid and non-destructive technique to detect the nutrients in the grains.

Among the numerous emerging technologies, hyperspectral imaging (HSI) is fast growing in quality detection because it can quickly obtain extensive information from the sample to quantify the variability in the surface properties and internal structures on both macro and microscopic levels (Luo et al., 2023; Pandey et al., 2023; Park et al., 2023). The HSI technology operates with a principle like other optical imaging techniques that rely on the interaction between the sample and the light (Wang et al., 2022a). The HSI prioritize the combination of the spectral and spatial information in which the series of data in every pixel of the image is equivalent to the spectral resolution of the image. In contrast, every spectral band holds spatial information at a specific wavelength (Jimoh and Hashim, 2024; Saha et al., 2023). The HSI technology has the advantage of a rapid, non-destructive, contamination-free and efficient mode of grain quality determination, which marks its ability to overcome the traditional methods in terms of time consumption, sample destruction, and labour-intensive. Several studies have applied the HSI in grain quality determination by utilizing a large amount of annotated which include moisture, protein and ash content of wheat (Chen et al., 2021), protein and physical traits of corn kernel (Varela et al., 2022), moisture and fatty acid in rice (Song et al., 2023) and moisture content of soybean (Guo et al., 2023b). Most of the studies considered the development of the HSI method as a non-destructive quality detection approach by collecting random samples across different varieties of grains (Wang et al., 2022b). However, the potential of applying HSI technology for evaluating grain quality detection under different conditions in a processing technique such as the drying process is scarcely available. Therefore, a three-stage processing technique was innovatively employed in using HSI for rapid detection of nutrient retention in the GR under different drying conditions. The three-stage process includes the evaluation of different preprocessing methods, selection of effective wavelengths, and model development, which was formed into a single processing train. The effective determination for the rapid detection of nutrient retention in the GR under different drying conditions through this method has a significant contribution to the timely control and improvement of the drying performance for effective high-quality grain production.

2. Materials and methods

2.1. Sample preparation and glutinous rice drying

Freshly harvested GR was supplied by Berkat Padi Sdn. Bhd., a local supplier of rice in Malaysia. Unwanted materials such as immature grains, broken grains, rice stalks, and foreign objects were removed from the healthy paddy using paddy cleaner. For the drying experiment, the GR was dried in a hot air box dryer (Model 3021, Malaysia). The dryer has an external dimension of 650 x 900 x 1900 and an internal dimension of 590 x 580 × 1400 mm. The heat is externally produced by 2.5 kW and distributed by the blower into the drying chamber through perforated media at ~1 m/s. The dryer was powered for about 60 min to ensure even heat distribution in the drying chamber before loading the GR samples into the dryer. The experiment was run at different temperatures of 50 °C, 60 °C and 70 °C and different grain layer thicknesses of 15 mm, 25 mm, 35 mm, and 45 mm, denoting a mass of 120 g, 190 g, 280 g and 380 g, respectively, and the experiment was performed in triplicate. The selection of temperature follows the range reported by Dey et al. (2024), Sadaka (2022) and Jimoh et al., (2024b), while the grain layer thicknesses were chosen by following the report of Mahfeli et al. (2022) on rice drying. For the rice milling, the dried GR was dehulled using a paddy huller (Satake, THU35B, Saitama, Japan) to obtain the brown rice. Using a paddy polisher (Satake TMO5C, Saitama, Japan), the brown rice was transformed into white rice by removing the rice bran. Subsequently, 72 samples of the polished grains were used for the hyperspectral image acquisition of the white GR, followed by the determination of the macronutrients of the grains.

2.2. Macronutrients determination by using reference method

The macronutrients in the milled GR which include protein content (PC), moisture content (MC), fat content (FC) and ash content (AC) were determined by using the Kjeldahl method, standard oven drying method, Soxhlet apparatus and furnace respectively.

2.2.1. Protein content

A Kjeldahl digester (Buchi, K-439 Model, Malaysia) was used to digest the mixture of 1g of the GR, 5g of Kjeldahl tab, and 20 ml of sulphuric acid H_2SO_4. After 4 h in the Kjeldahl digester, the colour of the mixture changed to pale yellow, indicating a complete digestion. The digested sample was distilled with a distillation system to recover the ammonia solution. After the distillation, the ammonia recovered was titrated with 0.2N H_2SO_4 solution, and the volume of the titrants was recorded. The *PC* of the sample was calculated using Equation (1) (Kaur and Asthir, 2021)

$$PC = \frac{(T_S - T_B) \times N \times F \times mN \times pf}{m \times 1000} \quad (1)$$

where *PC* is the protein content (%), T_S in the volume of the titrant for the sample (ml), T_B is the volume of titrant for blank (ml), N is the molar reaction factor ($H_2SO_4 = 2$), M is the concentration of the titrants, $m(N)$ is the molar weight of nitrogen (14.007 g/mol) and *pf* is the protein factor

2.2.2. Moisture content

The MC of the grains was measured by using standard oven drying. About 5 g of the GR was placed in the laboratory oven (Carbolite, PF60) at 105 °C for 24 h. The MC of the grains on a wet basis was calculated as the percentage of the weight loss to the initial weight of the samples, as expressed in Equation (2) (Qiao et al., 2022).

$$MC = \frac{W_s - W_d}{W_s} \times 100 \quad (2)$$

where MC is the moisture content (%), W_d is the weight of the sample after oven drying (g), and W_s is the weight of the sample (g).

2.2.3. Fat content

The FC of the GR was evaluated by dissolving the rice sample's fat in an organic solvent using the Soxhlet equipment. Subsequently, the solvent was evaporated from the fat extract using a rotary evaporator (Rasool et al., 2015). The dried weight (3g) sample was transferred to a thimble and the top was covered with a wad of fat-free cotton. The thimble was dropped into the fat extraction tube and coupled with a Soxhlet flask. A flask was filled with around 120 ml of petroleum ether. The top of the fat extraction tube was connected to the condenser. The material was extracted for 4 h at a temperature of 70–80 °C. After extraction, the thimble was withdrawn from the apparatus, and most of the ether was collected. The ether was evaporated using a rotary evaporator with low heat (50 °C). The flask was further dried at 100 °C for 1 h, and the difference in weights revealed the ether-soluble substance in the sample. The FC of the rice samples was calculated using Equation (3) (Kaur and Asthir, 2021; Verma and Srivastav, 2017).

$$FC = \frac{W_e}{W_s} \times 100 \quad (3)$$

where FC is the fat content (%), W_e is the weight of the extract (g) and W_s

is the weight of the sample (g).

2.2.4. Ash content

The AC of the selected sample was determined using the muffle furn. The clean, dry, and empty crucible was weighed using an electrical balance (±0.001 g). Three grams of GR were poured into the crucible, placed inside the muffle furnace, and fired at 600 °C for 5 h. After burning, the crucible was removed and cooled in a desiccator before weighing the crucible and ash. The AC of the rice samples was calculated using Equation (4) (Kaur and Asthir, 2021; Nath et al., 2022).

$$AC = \frac{W_a}{W_s} \tag{4}$$

where AC is the ash content (%), W_a is the weight of ash (g), and W_s is the weight of the sample (g).

2.3. Hyperspectral image acquisition and processing

The hyperspectral images of the milled GR were taken by using a visible near-infrared (Vis/NIR) HSI system setup. The system was set up in a low-light room to reduce the impact of light on the environment. Fig. 1 shows the schematic view of the setup for the HSI system. The components of the setup include a Vis/NIR-HSI camera (Cubert, S185 FireflEYE, Germany), a halogen lamp for lighting, a fan to cool the system and prevent overheating, a moveable platform, and a computer for managing, capturing, storing, and processing the hypercube image. For initial setup testing, the lighting position and camera height were manually adjusted to ensure a high-quality image was captured by the camera. The lighting source was at ~45 to plane and the camera was positioned at ~20 cm from the sample. The GR grains were placed in a 9 cm by 1.5 cm (diameter by height) Petri dish for image acquisition. The samples were then positioned on the setup platform for sequential hyperspectral image capturing. Calibration was performed using white and black reference images to lessen the impact of noise and dark current on the raw images. The white reference was measured using the Cubert white card (reflectance = 0.99) and the dark reference was recorded by shutting the lens cover of the camera. The HSI images were corrected by using the expression in Equation (5).

$$R = \frac{X - X_d}{X_w - X_d} \tag{5}$$

where R is the corrected image reflectance, X is the raw image sample,

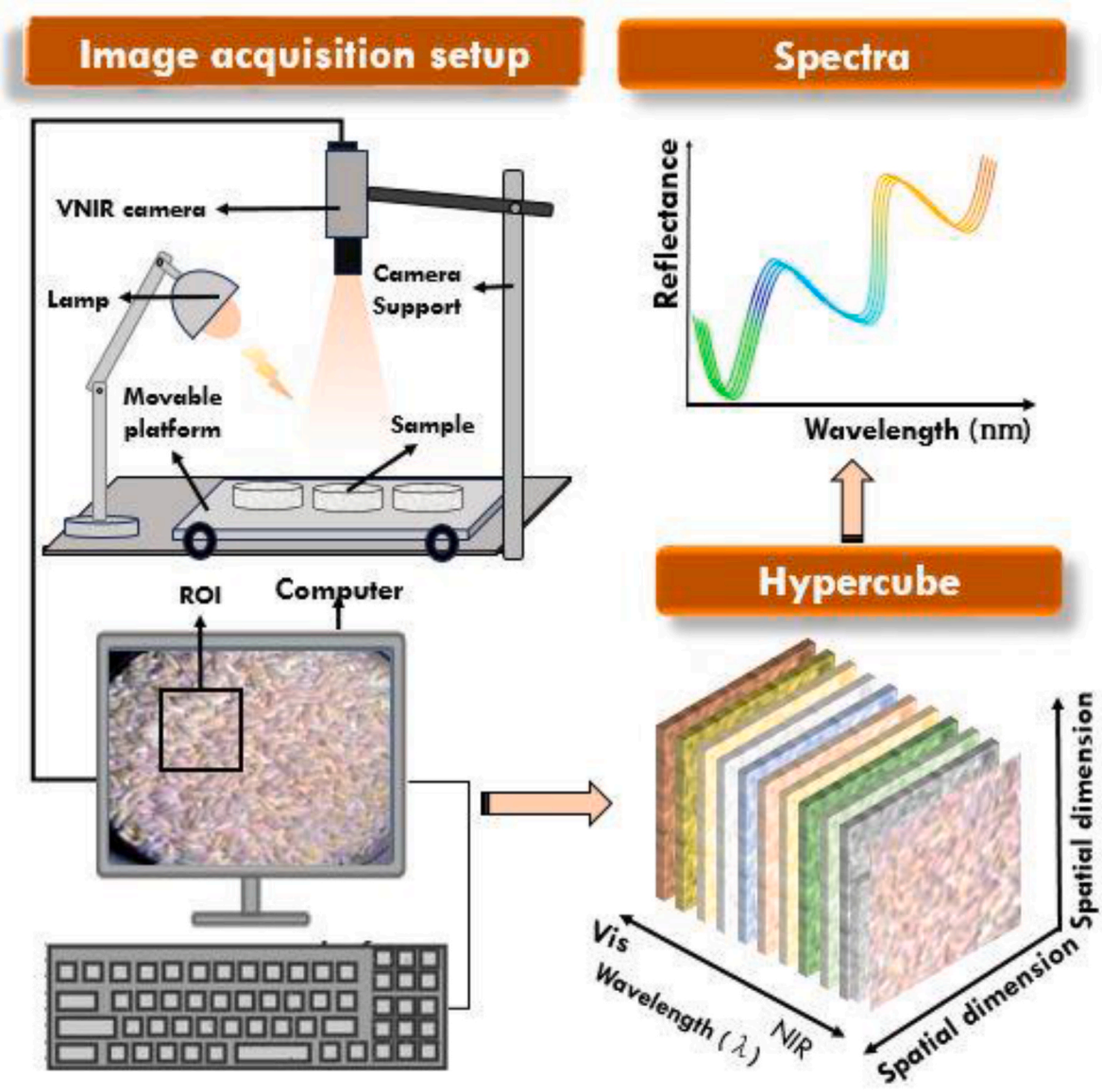

Fig. 1. The setup of the visible-near infrared hyperspectral imaging system.

X_w is the white reference image and X_d is the dark reference image.

The captured image has an output spatial resolution of 1000 × 1000 pixels and a spectral range of 450 nm–998 nm with a spectral bandwidth of 4 nm. The ROI was chosen using the HSI (Cubert Professional Software) program. The ROI of each image was selected as 200 by 200 pixels in a region with a high grain concentration and sufficient information to explain the macronutrients of the GR sample.

2.4. Spectral preprocessing

Different factors, such as instrument noise, stray light, and dark current could affect the original spectral data. To mitigate this effect, the spectral data were subjected to different spectral data correction techniques. Also, to increase the model's accuracy and predictive capacity of the model, spectral preprocessing is required to eliminate unnecessary information that is unrelated to the sample's characteristics (Panda et al., 2022; Tian et al., 2023). In this study, four preprocessing techniques that are often used in literature for the preprocessing of spectral data were applied to the HSI reflectance spectra. The Savitzky-Golay first derivative (SG1D) with five window sizes, standard normalized variate (SNV), moving window smoothing (MWS) with five window size, and multiplicative scattering correction (MSC) are all included in this method (Jimoh and Hashim, 2024; Kim et al., 2023; Marín-Méndez et al., 2024; Song et al., 2023). The raw spectra served as a benchmark for assessing how well the pre-processed approach worked throughout the model development process. By comparing the performance of these techniques based on predictive model accuracy, the best method was chosen for effective wavelength selection.

2.5. Effective wavelength selection

Hyperspectral images consist of many features with high dimensionality, multicollinearity and multiple redundant pieces of information that are time-consuming and complex to process (Song et al., 2023). The dimension of the entire spectral feature is decreased by choosing the effective wavelength. This approach eliminates redundant and unnecessary information and provides several advantages, including improving accuracy, processing speed, and real-time quality detection (Zhang et al., 2023a; Song et al., 2023; Zheng et al., 2018). To choose the effective wavelength features, this study employed the competitive adaptive reweighted sampling (CARS), random frog (RF), iteratively retains informative variables (IRIV), variable combination population analysis (VCPA), and variable iterative space shrinkage method (VISSA) (An et al., 2022; Ren et al., 2020; Zhang et al., 2023a). The effective wavelength selection was based on the adjudged best spectral preprocessing strategy. Therefore, the full preprocessed spectra were used as the benchmark to assess how the selection method affected the model's performance.

2.6. Partial Least Square Regression model development

Partial Least Square Regression (PLSR) is the conventional method for developing models while working with high multicollinearity and high dimensional data sets, such as HSI data (Xu et al., 2018). The PLSR condensed input variable (X) of the data set into several latent variables with the greatest amount of information while considering the variability in output variable (Y) and satisfies Equation (6) (Park et al., 2023)

$$Y = TP_t + E;\ X = TQ_t + F \tag{6}$$

where $T = (t_1, t_2, \ldots, t_n)$ is the variable; E and F are random errors of Y and X, respectively. In this study, the maximum latent variable was set as 10 with 5-fold cross-validation. To develop the PLSR predictive model, the total 72 collected data was split into the calibration and prediction data sets at a 3:1 ratio by using the Kennard-Stone (KS) technique, which maximizes the Euclidean distance between the system response to equally cover the multi-dimensional space. The larger part (75%) of the data set was used for calibrating the model. Understanding that model training is liable to overfit when using limited data, this study used cross-validation techniques to avoid overfitting and ensure model robustness and accuracy. The cross-validation techniques partition the calibration data set into multiple folds. The technique initially trains the model using a data fold and validates the model with other folds while correcting the models as the process is repeated for all the folds (Zhang et al., 2023a). To ensure accurate and effective prediction by the model, the prediction data set (25%) was used to test the reproducibility of the developed quantitative models (Achata et al., 2021).

2.7. Model accuracy indices

Computing the model performance indices such as root mean squared error (RMSE), coefficient of determination (R^2) and mean absolute percentage deviation (MAPD) are crucial phases of model development. In this study, Equation (5) and Equation (6), were used to calculate R^2 and RMSE, respectively, for both model calibration and prediction, while the MAPD, which further measures how well and reliably the model performed during prediction is determined using Equation (7). Consequently, the model with a higher R^2 with a lower RMSE and MAPD is considered the best model for the prediction of the macronutrients of GR (Guo et al., 2023b; Sun et al., 2019b).

$$R^2 = 1 - \frac{\sum_{i=1}^{n} \left(Y_{pre,i} - Y_{exp,i}\right)^2}{\sum_{i=1}^{n} \left(Y_{pre,i} - \overline{Y_{exp,i}}\right)^2} \tag{5}$$

$$RMSE = \sqrt{\frac{\sum_{i=1}^{n} \left(Y_{pre,i} - Y_{exp,i}\right)^2}{n}} \tag{6}$$

$$\text{MAPD} = \frac{1}{n} \sum_{i=1}^{n} \left| \frac{Y_{pre,i} - Y_{exp,i}}{Y_{pre,i}} \right| \times 100 \tag{7}$$

where $Y_{pre,i}$, is the predicted value of the GR quality, $Y_{exp,i}$ is the reference quality parameter of the GR, $\overline{Y_{exp,i}}$ is the reference quality parameter of the GR and n is the number of observations.

2.8. Visualization of the macronutrient distribution

In HSI, each image consists of a spectrum per pixel; therefore, the model developed for the determination of the macronutrient in each pixel was used to generate the spatial distribution map for the predicted macronutrient. The distribution map was plotted by following the procedure described by Ahmed et al. (2024) and Malegori et al. (2021). Each pixel macronutrient was predicted by employing the best predictive model that was developed based on the selected effective wavelength (SGID-VISSA-PLSR). Using the effective wavelength, the HSI image data cube was transformed into a two-dimensional vector, which was then subjected to the predictive model for macronutrient calculation. Subsequently, the generated one-dimensional vector was reshaped to create a coloured image with the identical spatial dimension as the initial data cube. Then, the distribution maps representing the macronutrient distribution were created using a pseudocolour plot with a linear colour scale. The computation of the preprocessing techniques, effective wavelength selection algorithm, the development of the corresponding model, and visualization of macronutrient distribution in this study were done on MATLAB 2023a software (Version 19.14.0, Mathwork. inc).

3. Results and discussions

3.1. Macronutrients in the glutinous rice

The result shows that the drying temperature and thickness significantly contributed to the variability in the quality of the milled GR. As shown in Fig. 2, The PC, MC, AC, and FC ranged from 4.67 ± 0.09% to 7.03 ± 0.26%, 12.05 ± 0.22% to 14.75 ± 0.12%, 0.4 ± 0.02% to 0.61 ± 0.02%, and 0.5 ± 0.03% to 1.55 ± 0.09% respectively. On average, the PC and MC were relatively reduced with the temperature, while the AC relatively increased. However, the MC of the GR grain shows the least significant ($P < 0.05$) variability with the drying conditions. This behaviour was mainly because the drying of the grains was controlled based on the gravimetric method to ensure a similar moisture level (12%) was attained after drying (Nath et al., 2022). For FC at thicknesses of 15 mm and 25 mm, the trend indicates a reduction in FC with increasing temperature. However, at thicknesses of 35 mm and 45 mm, the lowest FC was observed at 60 °C (0.5 ± 0.02% and 0.77 ± 0.04%, respectively). The values were significantly lower than those obtained at 50 °C and 70 °C. Compared to the literature, the PC falls within the range reported by Verma and Srivastav (2017) for non-aromatic rice (6.87 ± 0.10% to 7.09 ± 0.08%). Nevertheless, the values were slightly lower compared to the range of 7.23%–9.96% reported by Verma and Srivastav (2017) and Nath et al. (2022) for non-glutinous and aromatic rice. However, the MC (8.9%–13.57%), AC (0.35%–0.73%), and FC (0.06%–0.99%) reported by Rasool et al. (2015), Verma and Srivastav (2017), Kaur and Asthir (2021) and (Nath et al., 2022) were similar to the values in this study.

3.2. Hyperspectral reflectance

As stated earlier, the macronutrients retained in the milled GR vary significantly with the grain layer thickness and the temperature of the dryer. This section discusses the HSI reflectance curve as a non-destructive approach for detecting macronutrients in the GR grains. Using a 4 nm resolution sampling, the raw spectra of the images obtained from the HSI camera span 450–998 nm. The mean value of the reflectance curve for the pixels in the ROI of the sample is displayed in Fig. 3a. The reflectance value in all samples exhibits a decreasing trend from wavelength of 450 nm and reaches the absorbance valley between 490 and 520 nm. The subsequent absorption valley was found between 730 and 750 nm for most of the sample. This absorption valley is most likely associated with the third overtone C-H lengths and the second overtone O-H and N-H stretching vibration(Song et al., 2023). The third absorption valley range of 920–950 nm was located close to the absorption valley at 960 nm, which was caused by the second overtone O-H stretching linked to chemical composition (Qiao et al., 2022).

3.2.1. Spectral preprocessing method and model performance

The preprocessed reflectance spectral data under various processing methods are displayed in Fig. 3. Among the methods are MWS, SNV, MSC, and SG1D. The preprocessing technique was designed to lessen human, operational, instrumental, and environmental errors. The MWS minimized the noise and irregularities in the spectral data (Fig. 3b). The MSC lessens the spectral multiplicative and additive effects. To reduce the multiplicative and additive effects in the spectral data (Fig. 3d), the SNV uses the normalization approach (Fig. 3c). The spectral data to SG1D adjust the particle offset and scattering at the spectral baseline (Fig. 3e). The original full spectra, preprocessing spectra, and effective spectral bands served as the foundation for the development of the model.

3.2.2. Preprocess and model performance

The performance accuracy of the PLSR model combined with various preprocessing techniques for an efficient determination of the milled GR reference quality is summarised in Table 1. The best preprocessing method improves the predictive model's accuracy so that the reference macronutrient of the GR will be effectively detected, processed further, or deployed for use in real time (He et al., 2023). The RAW-PLSR model calibration had the R_C^2 of 0.9961, 0.9984, 0.9762, and 0.9917 with

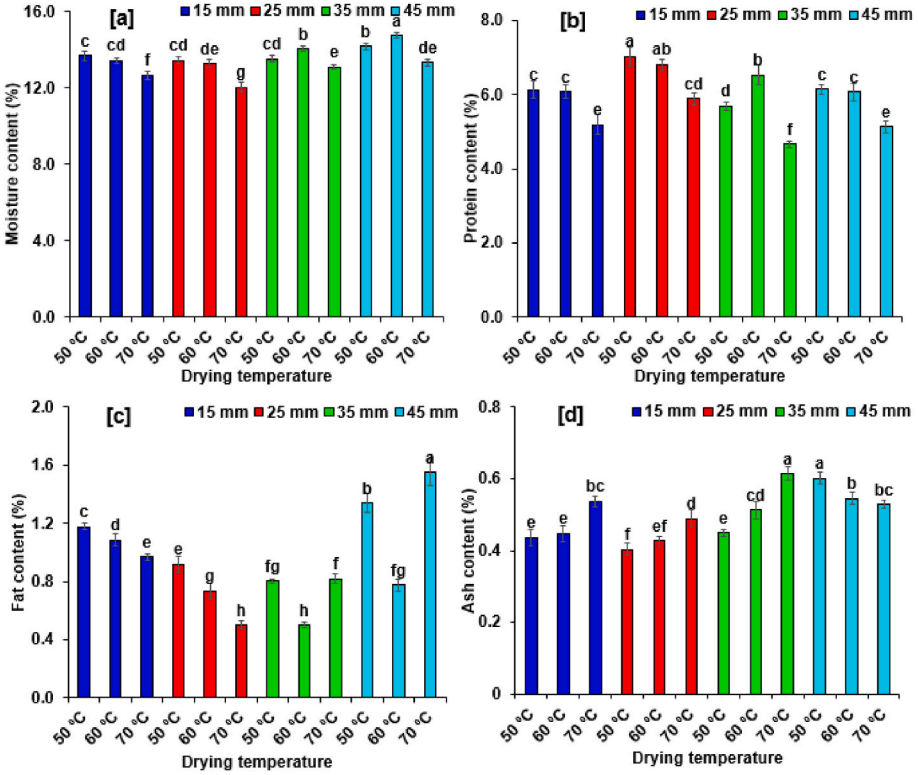

Fig. 2. Macronutrients retained in the milled GR under different drying conditions. a: MC, b: PC, c. FC, and d. AC.

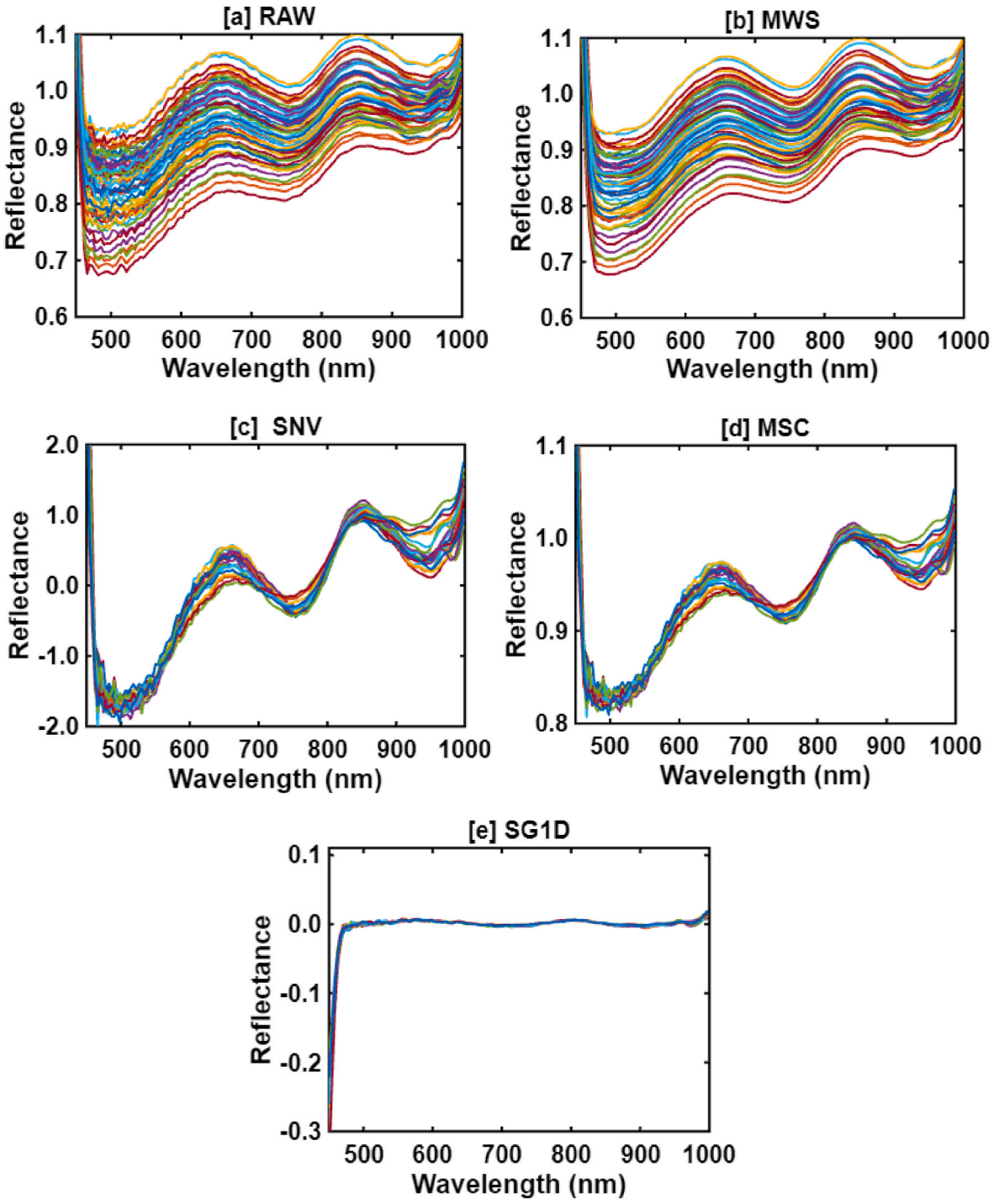

Fig. 3. Reflectance spectral data of milled GR: [a] RAW, [b] MWS, [c] SNV, [d] MSC, and [e] SG1D.

RMSEC of 0.0552, 0.0420, 0.0583, and 0.0108 for the PC, MC, FC, and AC, respectively. By using the RAW-PLSR model for the prediction data set, the R_P^2 of 0.6493, 0.9521, 0.4594 and 0.9773; RMSEP of 0.7205, 0.1942, 0.2408 and 0.0235 with MAPD of 7.00%, 1.21, 35.09, and 4.89% for the PC, MC, FC, and AC, respectively were obtained. Comparing all the preprocessing techniques, the SG1D-PLSR obtained the best performance for all the quality parameters of the GR. The SG1D-PLSR gave a compelling accuracy of $0.9963 \leq R_C^2 \leq 0.9974$, $0.0052 \leq RMSEC \leq 0.0524$, $0.9857 \leq R_P^2 \leq 0.9972$, $0.0043 \leq RMSEP \leq 0.0565$ and $0.34 \leq MAPD \leq 3.36$ Compared to the PLSR model of the original spectral (RAW-PLS), applying SG1D-PLS to the prediction dataset increases the accuracy of the model by 34.79%, 4.49%, 52.63% and 1.99% for PC, MC, FC and AC respectively. The linear relationship between the experimental and predicted value for the raw- and pre-processed spectra-based PLSR model is presented in Fig. A1. To improve the predictive model performance, the spectral data obtained from the SG1D preprocessed algorithm was selected for further processing (effective wavelength selection).

3.2.3. Feature selection accuracy

3.2.3.1. Competitive adaptive reweighted sampling. The CARS algorithm was preset to 50 Monte Carlo simulation sample sizes with 5-fold cross-

Table 1
Performance accuracy of the PLSR model coupled with different preprocessing methods.

Macronutrients	Preprocessing	R_C^2	RMSEC	R_P^2	RMSEP	MAPD (%)
PC	RAW	0.9961	0.0552	0.6493	0.7205	7.00
	MWS	0.9981	0.0419	0.6577	0.6037	5.87
	SNV	0.9997	0.0173	0.9700	0.1611	2.44
	MSC	0.9997	0.0169	0.9700	0.1611	2.44
	SG1D	0.9974	0.0459	0.9972	0.0557	0.69
MC	RAW	0.9984	0.0420	0.9521	0.1942	1.21
	MWS	0.9954	0.0681	0.9834	0.1366	0.80
	SNV	0.9998	0.0141	0.8986	0.3184	2.43
	MSC	0.9991	0.0283	0.8981	0.3191	2.44
	SG1D	0.9973	0.0524	0.9970	0.0565	0.34
FC	RAW	0.9762	0.0583	0.4594	0.2408	35.09
	MWS	0.9793	0.0577	0.8091	0.1105	9.93
	SNV	0.9907	0.0352	0.9863	0.0411	4.07
	MSC	0.9899	0.0366	0.9851	0.0428	4.24
	SG1D	0.9964	0.0234	0.9857	0.0293	3.36
AC	RAW	0.9817	0.0108	0.9773	0.0235	4.89
	MWS	0.9926	0.0073	0.9351	0.0239	3.87
	SNV	0.9979	0.0040	0.9778	0.0128	2.43
	MSC	0.9979	0.0040	0.9778	0.0127	2.43
	SG1D	0.9963	0.0052	0.9972	0.0043	0.74

validation for model evaluation. Under different simulation runs, Figs. A2a–d shows the resulting variation in the root mean square error progression for cross-validation (RMSECV). The minimum RMSECV was obtained at 19, 13, 22, and 22 iterations for the PC, MC, FC, and AC, respectively. The RMSECV value was 0.078 for PC, 0.089 for MC, 0.0151 for FC, and 0.031 for AC. The number of wavelengths retained by the CARS algorithm at the optimal selection point of 19, 13, 22, and 22 were 29 bands for PC, 49 bands for MC, 22 for the FC and 22 bands for AC. The number of selected wavelengths is equivalent to a pronounced reduction of 78.99%, 64.49%, 84.06%, and 86.06% compared to the full wavelength of PC, MC, FC, and AC, respectively (Figs. A2e–h).

3.2.3.2. Random frog. For the parameters of the RF algorithm, the number of Monte Carlo simulations was set to 1000 with a minimum of 2 features at the initial sampling point, and the regression coefficient was used for variable index assessment. Figs. A3(a–d) presents the variation in the RMSEP for all the Monte Carlo simulated samples of the RF computation algorithm. Selecting the variable in the RF simulation with the lowest RMSEP in the final stage gave a value of 0.838, 0.078, 0.024 and 0.003 for the PC, MC, FC, and AC, respectively. The algorithm selects 19, 41, 17, and 41 bands as the effective wavelength for the PC, MC, FC, and AC, which amount to 86.23%, 70.29%, 87.68% and 70.29% reduction in the whole wavelength, respectively (Figs. A3e–h).

3.2.3.3. Iteratively retains informative variables. Figs. A4(a–d) shows the variation in the remaining variable with the iteration round of the IRIV algorithm during computation for the PC, MC, FC and AC of GR, respectively. The session of variable selection was completed in 6 iterations for PC, MC, and FC of the GR, and AC was attained in 7 iterations. The selected wavelength was reduced continuously until the final round. In the initial three rounds of iteration, more than 50% of bands were eliminated for all quality parameters. Subsequently, the rate of band removal stabilized, with 3–14 wavelengths being removed through backward elimination in the final iteration round (Figs. A4a–d). This left approximately 18.12%, 13.04%, 19.57%, and 29.71% of the total wavelengths selected for PC, MC, FC, and AC, respectively, representing 25, 18, 27, and 41 selected wavelengths (Figs. A4e–h).

3.2.3.4. Variable combination population analysis. The RMSECV progression during the iterations in the exponential decreasing function (EDF) for the VCPA computation algorithm is shown in Figs. A5(a–d) for the PC, MC, FC and AC of GR. The characteristic space shrunk, and RMSECV depicted a continuous downward trend with the repeated operation of EDF. In the variable selection process, the VCPA run with the lowest RMSECV in the final stage yielded values of 0.065, 0.065, 0.032, and 0.002 for the PC, MC, FC, and AC, respectively. Subsequently, 10, 11, 11, and 10 bands were identified as effective wavelengths for the PC, MC, FC, and AC, representing a reduction of 92.75%,

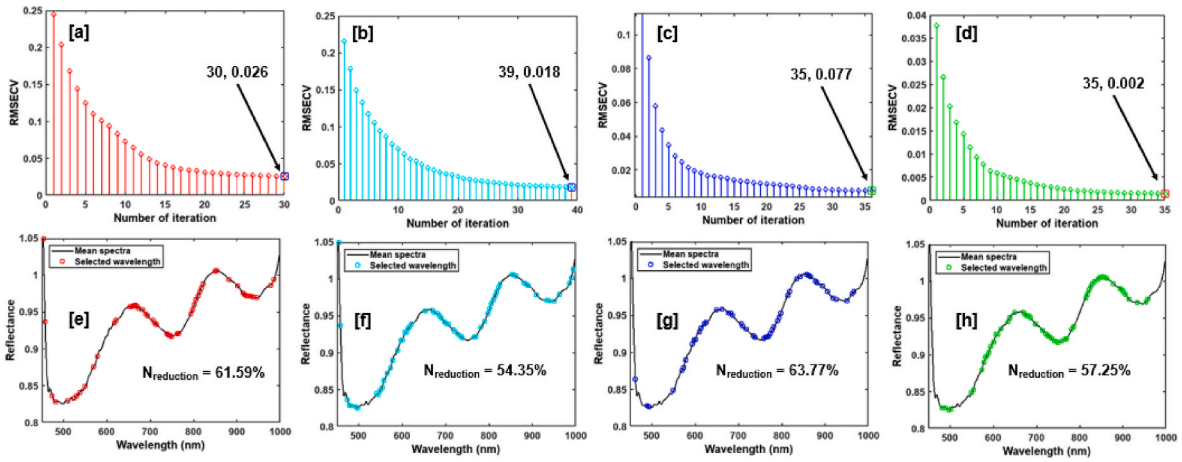

Fig. 4. Result of effective wavelength selection of the VISSA algorithm. [a], [b], [c] and [d] represent the RMSECV at different numbers of iterations for PC, MC, FC and AC respectively. [e], [f], [g] and [h] represent the selected wavelength and percentage reduction of wavelength for PC, MC, FC and AC respectively.

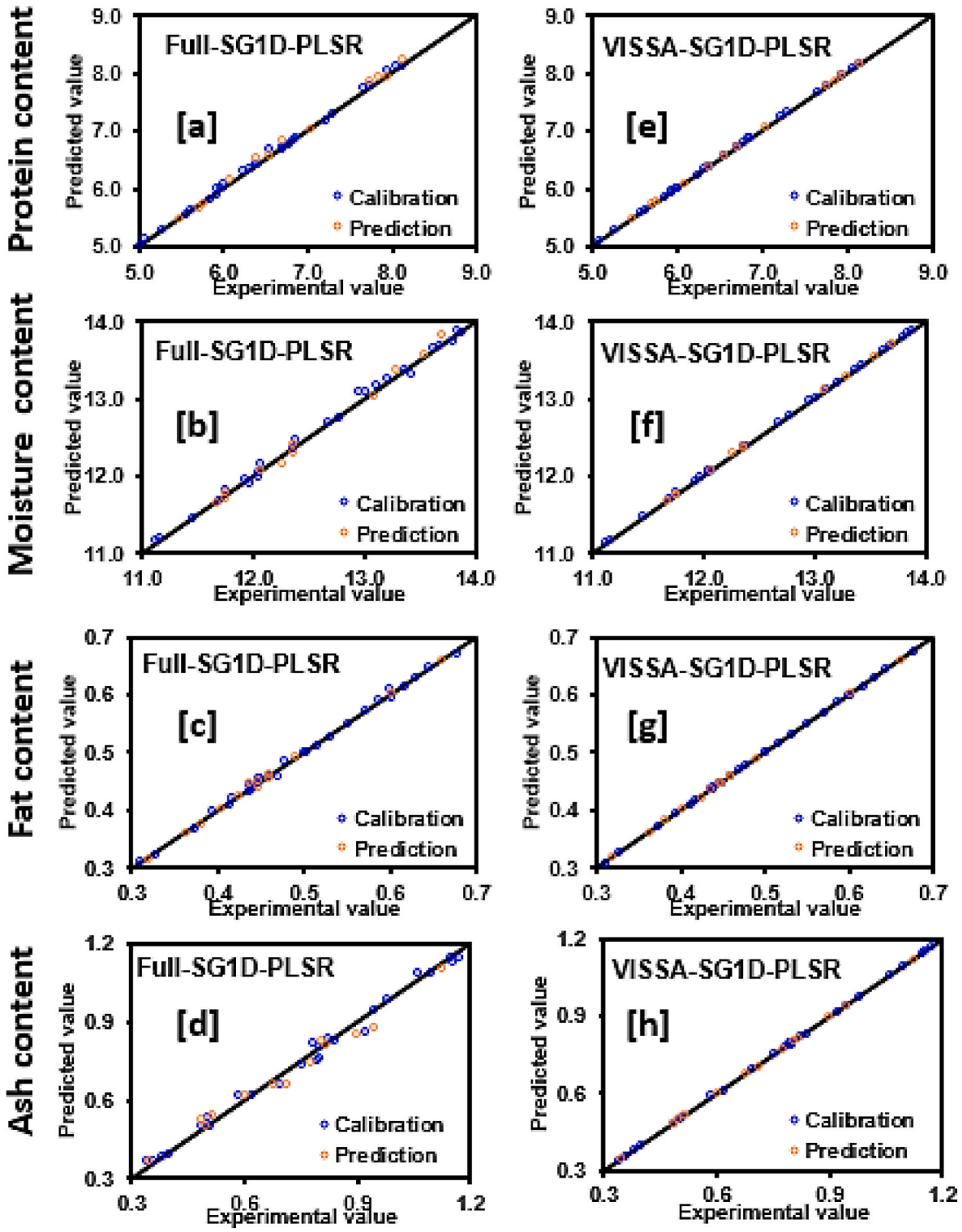

Fig. 5. The linear relationship between the experimentally obtained value and the predicted value of the processing sequence for the PLSR model based on the Full spectral (a–d) and best preprocessing method (e–h).

92.03%, 92.03%, and 92.75% in the total number of wavelengths, respectively (Figs. A5e–h).

3.2.3.5. Variable iterative space shrinkage approach. Fig. 4a–d shows the RMSECV variation at different iteration numbers during computation with the VISSA algorithm. For the PC, MC, FC, and AC of the GR, 30, 39, 36, and 35 iterations were conducted, respectively, with each achieving minimum RMSECV values of 0.026, 0.018, 0.077, and 0.002. The final bands selected by the VISSA algorithm after the iteration rounds are depicted in Fig. 4(a–d) for the PC, MC, FC, and AC of GR, respectively. A total of 53, 62, 50, and 59 bands were selected for the PC, MC, FC, and AC, indicating reductions of 61.59%, 55.07%, 63.77%, and 57.25% in the full wavelength, as shown in Fig. 4e–h.

3.2.4. Comparison of model accuracy

Table 2 summarises the result of the predictive model performance by comparing the inclusion of different effective wavelength selection techniques to the selected model with the best preprocessing method (SG1D-PLSR). The linear relationship between the experimentally obtained value and the predicted value of the selected best effective wavelength-based and full spectral-based PLSR model is shown in Fig. 5. All the effective wavelength selection techniques fall within the acceptable limit based on prediction accuracy and precision. All the methods except VCPA gave a decent performance, which was higher than that of using full spectral (SG1D-Full-PLSR). Although the VCPA has the highest wavelength reduction (>90%) when compared to full spectral, the SG1D-VCPA-PLSR reduced the accuracy by 1.03%, 3.47%, 2.11%, and 2.05% for the PC, MC, FC, and AC, respectively. For all the quality parameters, the SG1D-VISSA-PLSR model attained 100% accuracy during the calibration and prediction with $0.0005 \leq RMSE \leq 0.0045$ and $0.0005 \leq RMSE \leq 0.0035$ respectively. This model had the most significant improvement compared to the accuracy of SG1D-Full-PLSR, which ranged from 99.63% to 99.74% and 98.57%–99.72% for calibration and prediction, respectively. Therefore, the combination of the SG1D preprocessing method and VISSA effective wavelength selection techniques (SG1D-VISSA-PLSR model) was considered the best processing sequence. In a similar study by Zhang et al. (2022b), the FC of maize was determined using HSI, achieving an accuracy of 91.98%. Song et al. (2023) demonstrated the effectiveness of CARS-PLSR in predicting moisture for rice samples using an HSI system, achieving an accuracy of 0.9643, and 0.0032 for R_P^2, and RMSEP, respectively. Mansuri et al. (2022) utilized Vis/NIR-HSI to determine fungal contamination in maize, achieving an accuracy of over 95%. Guo et al. (2023b) determined the MC of soybean seed with a prediction accuracy of R_p^2 of 97.13% by using a Vis/NIR-HSI system. Aulia et al. (2022) determined the PC of soybean with a prediction accuracy of 92% using near-infrared HSI. Sun et al. (2019b) determined the MC of peanut kernels using HSI, achieving an accuracy of 93.63%.

3.3. Macronutrient visualization

The accuracy of the developed model has a significant bearing on the dependability and correctness of the distribution maps. Using a wrong model could provide false information about the spatial distribution, which could have a detrimental effect on how the distribution map and its implications are interpreted (Ahmed et al., 2024). Therefore, creating a distribution map is another way of ensuring the model prediction accuracy by visualizing the spatial variation of the response. Fig. 6 illustrates the selected GR sample with high, medium, and low values of the tested macronutrients. Based on the best predictive model developed from the selected effective wavelength (VISSA-PLSR), the map was used to depict the distribution of the macronutrient distribution in GR. The visualization accuracy is relative to the performance of the developed model, it can be assessed based on the colour scale. The application of a linear colour scale for mapping the micronutrient guarantees that the pixels with the same predicted macronutrient values are depicted with comparable colour characteristics when mapping the variation in the macronutrient retained in the GR. The relative distribution of the PC, MC, AC, and FC is thus represented by the corresponding pixel value, as seen in Fig. 6a to d, respectively. The macronutrient distribution map not only illustrates the variations in micronutrients at the pixel level but also shows how HSI may be used to reveal the pixel-wise chemical constituent, which may be difficult to accomplish with RGB image and unaided human vision. Consequently, an essential application of optical images in grain processing is the use of HSI to map the spatial distribution of the grain quality parameters.

4. Conclusion

In this study, Vis/NIR HSI coupled with different spectral preprocessing (MWS, SNV, MSC, and SG1D) and effective wavelength selection techniques (CARS, IRIV, RF, VCPA and VISSA) for the detection of macronutrients retained in GR under different drying conditions. Subsequently, predictive models were developed based on processed spectra to rapidly detect the macronutrients, including PC, MC, FC and AC. The result shows the spectral preprocess with the SG1D method has the highest performance with the best accuracy of $0.9963 \leq R_C^2 \leq 0.9974$, $0.0052 \leq RMSEC \leq 0.0524$, $0.9857 \leq R_P^2 \leq 0.9972$, $0.0043 \leq RMSEP \leq 0.0565$ and $0.34 \leq MAPD \leq 3.36$. Compared to the RAW-PLSR, the SG1D-PLSR increases the model accuracy for the prediction dataset by 34.79%, 4.49%, 52.63% and 1.99% for PC, MC, FC and AC, respectively. Using the VISSA technique for effective wavelength selection reduces the total number of wavelengths by over 60%. This method increases the accuracy of the model (SG1D-VISSA-PLSR) to 100% for both model

Table 2
Summary of the performance predictive model under different effective wavelength selection techniques.

Quality	Model	Wavelength selection	R_C^2	RMSEC	R_P^2	RMSEP	MAPD (%)
PC	SG1D-PLSR	Full	0.9974	0.0459	0.9972	0.0557	0.69
		CARS	0.9997	0.0161	0.9997	0.0177	0.21
		IRIV	0.9971	0.0489	0.9968	0.0601	0.79
		RF	0.9999	0.0122	0.9997	0.0148	0.20
		VCPA	0.9907	0.0879	0.9868	0.1256	1.07
		VISSA	1.0000	0.0047	1.0000	0.0035	0.03
MC	SG1D-PLSR	Full	0.9973	0.0524	0.9970	0.0565	0.34
		CARS	0.9995	0.0217	0.9996	0.0197	0.12
		IRIV	0.9984	0.0398	0.9976	0.0526	0.33
		RF	0.9993	0.0249	0.9994	0.0254	0.16
		VCPA	0.9657	0.1855	0.9622	0.1856	1.14
		VISSA	1.0000	0.0033	1.0000	0.0020	0.01
FC	SG1D-PLSR	Full	0.9964	0.0234	0.9857	0.0293	3.36
		CARS	0.9996	0.0084	0.9986	0.0088	0.81
		IRIV	0.9965	0.0230	0.9883	0.0252	2.81
		RF	0.9981	0.0115	0.9996	0.0082	0.81
		VCPA	0.9833	0.0507	0.9646	0.0470	5.07
		VISSA	1.0000	0.0023	1.0000	0.0014	0.13
AC	SG1D-PLSR	Full	0.9963	0.0052	0.9972	0.0043	0.74
		CARS	0.9998	0.0012	0.9998	0.0012	0.17
		IRIV	0.9996	0.0018	0.9996	0.0018	0.30
		RF	0.9991	0.0024	0.9995	0.0019	0.28
		VCPA	0.9847	0.0107	0.9767	0.0125	1.96
		VISSA	1.0000	0.0005	1.0000	0.0005	0.07

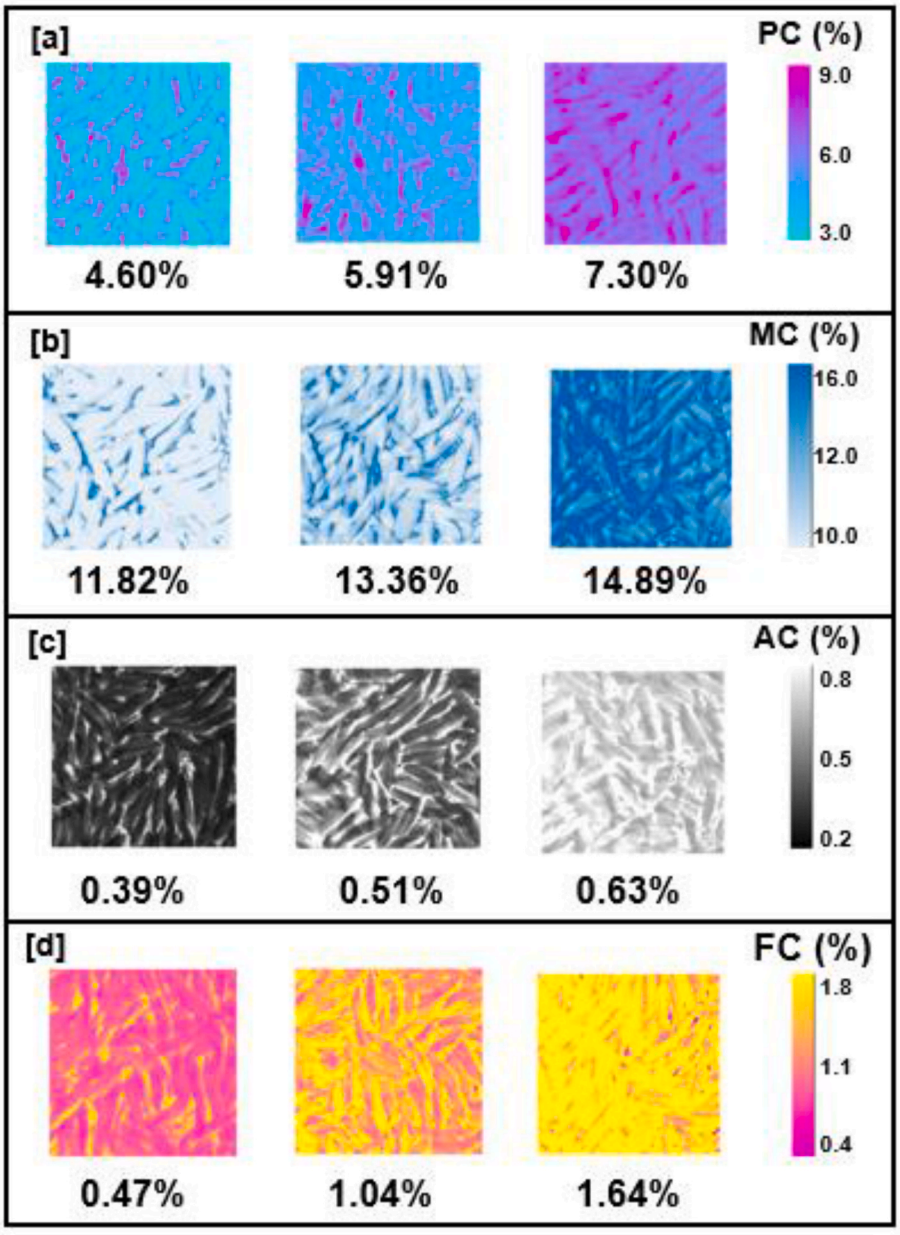

Fig. 6. Distribution of the macronutrient in the GR. [a]: PC, [b]: MC, [c]: AC and [d]: FC.

calibration and training. Subsequently, the macronutrient distribution of GR was effectively visualized by using a chemical colour map based on the best predictive model. Although the predictive model gave a good performance, further improvement could study a wider range of quality determination, and consider the variability of macronutrients with other factors such as dryer type, air velocity and air humidity. Also, further studies could evaluate HSI techniques with higher wavelengths such as short-wave far infrared. Since this study is specifically conducted for GR, it is crucial to recalibrate the developed model before adopting it for other rice varieties. However, the developed SG1D-VISSA-PLSR model is suggested for effective and rapid detection of macronutrients in GR grains on both small and industrial scales based on near-infrared hyperspectral imaging. Technological industries can adopt the model as a reliable basis for building a smart and reliable spectral system for rapid detection of the macronutrients in GR.

CRediT authorship contribution statement

Kabiru Ayobami Jimoh: Conceptualization. **Norhashila Hashim:** Conceptualization. **Rosnah Shamsudin:** supervised and provided critical discussion and contribution to the manuscript revision. **Hasfalina Che Man:** supervised and provided critical discussion and contribution to the manuscript revision. **Mahirah Jahari:** supervised and provided critical discussion and contribution to the manuscript revision. **Puteri Nurain Megat Ahmad Azman:** collected the data. **Daniel I. Onwude:** provided critical discussion and contribution to the manuscript revision.

Declaration of competing interest

The authors declare that they have no known competing financial interests or personal relationships that could have appeared to influence the work reported in this paper.

Acknowledgements

The authors acknowledge the financial support of the Ministry of Higher Education, Malaysia, through the Transdisciplinary Research Grant Scheme Project (TRGS/1/2020/UPM/02/7).

Appendix A. Supplementary data

Supplementary data to this article can be found online at https://doi.org/10.1016/j.crfs.2024.100963.

Data availability

Data will be made available on request.

References

Achata, E.M., Esquerre, C., Ojha, K.S., Tiwari, B.K., O'Donnell, C.P., 2021. Development of NIR-HSI and chemometrics process analytical technology for drying of beef jerky. Innovative Food Sci. Emerging Technol. 69, 102611. https://doi.org/10.1016/j.ifset.2021.102611.

Ahmed, T., Wijewardane, N.K., Lu, Y., Jones, D.S., Kudenov, M., Williams, C., Villordon, A., Kamruzzaman, M., 2024. Advancing sweetpotato quality assessment with hyperspectral imaging and explainable artificial intelligence. Comput. Electron. Agric. 220 (January), 108855. https://doi.org/10.1016/j.compag.2024.108855.

An, T., Yu, S., Huang, W., Li, G., Tian, X., Fan, S., Dong, C., Zhao, C., 2022. Robustness and accuracy evaluation of moisture prediction model for black tea withering process using hyperspectral imaging. Spectrochimica Acta - Part A: Molecular and Biomolecular Spectroscopy 269, 120791. https://doi.org/10.1016/j.saa.2021.120791.

Aulia, R., Kim, Y., Zuhrotul Amanah, H., Muhammad Akbar Andi, A., Kim, H., Kim, H., Lee, W.H., Kim, K.H., Baek, J.H., Cho, B.K., 2022. Non-destructive prediction of protein contents of soybean seeds using near-infrared hyperspectral imaging. Infrared Phys. Technol. 127 (June), 104365. https://doi.org/10.1016/j.infrared.2022.104365.

Buresova, I., Cervenka, L., Sebestikova, R., Augustova, M., Jarosova, A., 2023. Applicability of flours from Pigmented and glutinous rice in gluten-free Bread Baking. Foods 12 (6), 1–13. https://doi.org/10.3390/foods12061324.

Chen, X., Siesler, H.W., Yan, H., 2021. Rapid analysis of wheat flour by different handheld near-infrared spectrometers: a discussion of calibration model maintenance and performance comparison. Spectrochimica Acta - Part A: Molecular and Biomolecular Spectroscopy 252, 119504. https://doi.org/10.1016/j.saa.2021.119504.

Coradi, P.C., Maldaner, V., Lutz, É., da Silva Daí, P.V., Teodoro, P.E., 2020. Influences of drying temperature and storage conditions for preserving the quality of maize postharvest on laboratory and field scales. Sci. Rep. 10 (1), 1–15. https://doi.org/10.1038/s41598-020-78914-x.

Dey, B., Jayaraman, S., Balasubramanian, P., 2024. Investigating the effects of drying on the physical properties of Kombucha Bacterial Cellulose: Kinetic study and modeling approach. J. Clean. Prod. 452 (April), 142204. https://doi.org/10.1016/j.jclepro.2024.142204.

Dibagar, N., Amiri, R., Figiel, A., Ghasemi, A., 2022. A modeling strategy for hot drying of rough rice assisted by ultrasonic wave. Food Bioprod. Process. 132, 114–129. https://doi.org/10.1016/j.fbp.2022.01.004.

Ding, C., Zhang, H., Zhao, S., Luo, Y., Hu, Q., Liu, Q., Tian, T., Zhang, L. jie, Xue, X., 2022. Efficiency, functionality, and multi-scale structure of citric acid esterified glutinous rice starch synthesized via infrared radiation. Food Hydrocolloids 125, 107377. https://doi.org/10.1016/j.foodhyd.2021.107377.

Guo, Z., Zhang, J., Ma, C., Yin, X., Guo, Y., Sun, X., Jin, C., 2023. Application of visible-near-infrared hyperspectral imaging technology coupled with wavelength selection algorithm for rapid determination of moisture content of soybean seeds. J. Food Compos. Anal. 116 (June 2022), 105048. https://doi.org/10.1016/j.jfca.2022.105048.

He, H.J., Wang, Y., Ou, X., Ma, H., Liu, H., Yan, J., 2023. Rapid determination of chemical compositions in chicken flesh by mining hyperspectral data. J. Food Compos. Anal. 116 (September 2022), 105069. https://doi.org/10.1016/j.jfca.2022.105069.

Jimoh, K.A., Hashim, N., 2024. Recent advances in non-invasive techniques for assessing food quality : Applications and innovations. In: Advances in Food and Nutrition Research. Elsevier. https://doi.org/10.1016/bs.afnr.2024.09.006.

Jimoh, K.A., Hashim, N., Shamsudin, R., Che, H., Jahari, M., Eka, R., 2024a. Understanding the evolution of moisture during isothermal dehydration of glutinous rice through global sensitivity analysis. Innovative Food Sci. Emerging Technol. 95, 103733. https://doi.org/10.1016/j.ifset.2024.103733.

Jimoh, K.A., Hashim, N., Shamsudin, R., Man, H.C., Jahari, M., 2023a. Recent advances of optical imaging in the drying process of grains – a review. J. Stored Prod. Res. 103, 102145. https://doi.org/10.1016/j.jspr.2023.102145.

Jimoh, K.A., Hashim, N., Shamsudin, R., Man, H.C., Jahari, M., 2024b. Optimization of computational intelligence approach for the prediction of glutinous rice dehydration. J. Sci. Food Agric. https://doi.org/10.1002/jsfa.13445.

Jimoh, K.A., Hashim, N., Shamsudin, R., Man, H.C., Jahari, M., Onwude, D.I., 2023b. Recent Advances in the drying process of grains. Food Eng. Rev. https://doi.org/10.1007/s12393-023-09333-7.

Kaur, M., Asthir, B., 2021. Characterization of biochemical and proximate composition in rice grains as influenced by germination. Cereal Res. Commun. 49 (2), 291–299. https://doi.org/10.1007/s42976-020-00101-5.

Kim, Y.K., Qin, J., Baek, I., Lee, K.M., Kim, S.Y., Kim, S., Chan, D., Herrman, T.J., Kim, N., Kim, M.S., 2023. Detection of aflatoxins in ground maize using a compact and automated Raman spectroscopy system with machine learning. Curr. Res. Food Sci. 7 (November), 100647. https://doi.org/10.1016/j.crfs.2023.100647.

Komolafe, C. A., Mumuni, F., Jimoh, K. A., & Akendola, F. A. (2025). Kinetics and modeling of the heat and mass transfer during the solar drying of Cassava Slices under Natural Convection mode. J. Therm. Sci. Eng. Appl., 17, 1–12. https://doi.org/10.1115/1.4066694.

Li, Y., Ding, G., Yokoyama, W., Zhong, F., 2018. Characteristics of annealed glutinous rice flour and its formation of fast-frozen dumplings. J. Cereal. Sci. 79, 106–112. https://doi.org/10.1016/j.jcs.2017.09.016.

Liu, S., Zhang, H., Peng, J., Yao, Z., Han, X., Liu, T., Zhang, S., Mao, J., 2023. Effects of degree of milling on japonica and glutinous rice used for huangjiu brewing physicochemical properties. Lwt 183 (April), 114825. https://doi.org/10.1016/j.lwt.2023.114825.

Luo, W., Zhang, J., Huang, H., Peng, W., Gao, Y., Zhan, B., Zhang, H., 2023. Prediction of fat content in salmon fillets based on hyperspectral imaging and residual attention convolution neural network. Lwt 184 (May), 115018. https://doi.org/10.1016/j.lwt.2023.115018.

Mahfeli, M., Zarein, M., Zomorodian, A., Khafajeh, H., 2022. Investigation of rice performance characteristics: a comparative study of LR, ANN, and RSM. Food Sci. Nutr. 10 (10), 3501–3514. https://doi.org/10.1002/fsn3.2953.

Malegori, C., Oliveri, P., Mustorgi, E., Boggiani, M.A., Pastorini, G., Casale, M., 2021. An in-depth study of cheese ripening by means of NIR hyperspectral imaging: spatial mapping of dehydration, proteolysis and lipolysis. Food Chem. 343 (November 2020), 128547. https://doi.org/10.1016/j.foodchem.2020.128547.

Mansuri, S.M., Chakraborty, S.K., Mahanti, N.K., Pandiselvam, R., 2022. Effect of germ orientation during Vis-NIR hyperspectral imaging for the detection of fungal contamination in maize kernel using PLS-DA, ANN and 1D-CNN modelling. Food Control 139 (December 2021), 109077. https://doi.org/10.1016/j.foodcont.2022.109077.

Marín-Méndez, J.J., Luri Esplandiú, P., Alonso-Santamaría, M., Remirez-Moreno, B., Urtasun Del Castillo, L., Echavarri Dublán, J., Almiron-Roig, E., Sáiz-Abajo, M.J., 2024. Hyperspectral imaging as a non-destructive technique for estimating the nutritional value of food. Curr. Res. Food Sci. 9 (March). https://doi.org/10.1016/j.crfs.2024.100799.

Nath, S., Bhattacharjee, P., Bhattacharjee, S., Datta, J., Dolai, A.K., 2022. Grain characteristics, proximate composition, phytochemical capacity, and mineral content of selected aromatic and non-aromatic rice accessions commonly cultivated in the North-East Indian plain belt. Applied Food Research 2 (1), 100067. https://doi.org/10.1016/j.afres.2022.100067.

Panda, B.K., Mishra, G., Ramirez, W.A., Jung, H., Singh, C.B., Lee, S.H., Lee, I., 2022. Rancidity and moisture estimation in shelled almond kernels using NIR hyperspectral imaging and chemometric analysis. J. Food Eng. 318, 110889. https://doi.org/10.1016/j.jfoodeng.2021.110889.

Pandey, P., Veazie, P., Whipker, B., Young, S., 2023. Predicting foliar nutrient concentrations and nutrient deficiencies of hydroponic lettuce using hyperspectral imaging. Biosyst. Eng. 230, 458–469. https://doi.org/10.1016/j.biosystemseng.2023.05.005.

Park, S., Yang, M., Yim, D.G., Jo, C., Kim, G., 2023. VIS/NIR hyperspectral imaging with artificial neural networks to evaluate the content of thiobarbituric acid reactive substances in beef muscle. J. Food Eng. 350 (September 2022), 111500. https://doi.org/10.1016/j.jfoodeng.2023.111500.

Qiao, M., Xu, Y., Xia, G., Su, Y., Lu, B., Gao, X., Fan, H., 2022. Determination of hardness for maize kernels based on hyperspectral imaging. Food Chem. 366 (March 2021), 130559. https://doi.org/10.1016/j.foodchem.2021.130559.

Rasool, N., Baba, W.N., Muzzaffar, S., Masoodi, F.A., Ahmad, M., Munaff Bhat, M., 2015. A correlation study of proximate composition, physical and cooking properties of new high yielding and disease resistant rice varieties. Cogent Food Agric. 1 (1). https://doi.org/10.1080/23311932.2015.1099175.

Ren, G., Ning, J., Zhang, Z., 2020. Intelligent assessment of tea quality employing visible-near infrared spectra combined with a hybrid variable selection strategy. Microchem. J. 157, 105085. https://doi.org/10.1016/j.microc.2020.105085.

Sadaka, S., 2022. Impact of grain layer thickness on rough rice drying kinetics parameters. Case Stud. Therm. Eng. 35, 102026. https://doi.org/10.1016/j.csite.2022.102026.

Saha, D., Senthilkumar, T., Sharma, S., Singh, C.B., Manickavasagan, A., 2023. Application of near-infrared hyperspectral imaging coupled with chemometrics for rapid and non-destructive prediction of protein content in single chickpea seed. J. Food Compos. Anal. 115 (June 2022), 104938. https://doi.org/10.1016/j.jfca.2022.104938.

Song, Y., Cao, S., Chu, X., Zhou, Y., Xu, Y., Sun, T., Zhou, G., Liu, X., 2023. Non-destructive detection of moisture and fatty acid content in rice using hyperspectral imaging and chemometrics. J. Food Compos. Anal. 121 (May), 105397. https://doi.org/10.1016/j.jfca.2023.105397.

Sun, J., Shi, X., Zhang, H., Xia, L., Guo, Y., Sun, X., 2019b. Detection of moisture content in peanut kernels using hyperspectral imaging technology coupled with chemometrics. J. Food Process. Eng. 42 (7), 1–10. https://doi.org/10.1111/jfpe.13263.

Tian, P., Meng, Q., Wu, Z., Lin, J., Huang, X., Zhu, H., Zhou, X., Qiu, Z., Huang, Y., Li, Y., 2023. Detection of mango soluble solid content using hyperspectral imaging technology. Infrared Phys. Technol. 129. https://doi.org/10.1016/j.infrared.2023.104576.

Tu, Q., Ma, Z., Wang, H., 2023. Investigation of wet particle drying process in a fluidized bed dryer by CFD simulation and experimental measurement. Chem. Eng. J. 452, 139200. https://doi.org/10.1016/j.cej.2022.139200.

Varela, J.I., Miller, N.D., Infante, V., Kaeppler, S.M., de Leon, N., Spalding, E.P., 2022. A novel high-throughput hyperspectral scanner and analytical methods for predicting maize kernel composition and physical traits. Food Chem. 391 (December 2021), 133264. https://doi.org/10.1016/j.foodchem.2022.133264.

Verma, D.K., Srivastav, P.P., 2017. Proximate composition, mineral content and fatty acids Analyses of aromatic and non-aromatic Indian rice. Rice Sci. 24 (1), 21–31. https://doi.org/10.1016/j.rsci.2016.05.005.

Wang, Z., Fu, Z., Weng, W., Yang, D., Wang, J., 2022a. An efficient method for the rapid detection of industrial paraffin contamination levels in rice based on hyperspectral imaging. LWT - Food Sci. Technol. (Lebensmittel-Wissenschaft -Technol.) 171 (November).

Wang, Z., Fu, Z., Weng, W., Yang, D., Wang, J., 2022b. An efficient method for the rapid detection of industrial paraffin contamination levels in rice based on hyperspectral imaging. Lwt 171 (June), 114125. https://doi.org/10.1016/j.lwt.2022.114125.

Xu, D., Ma, W., Chen, S., Jiang, Q., He, K., Shi, Z., 2018. Assessment of important soil properties related to Chinese Soil Taxonomy based on vis–NIR reflectance spectroscopy. Comput. Electron. Agric. 144, 1–8. https://doi.org/10.1016/j.compag.2017.11.029.

Zhang, L., An, D., Wei, Y., Liu, J., Wu, J., 2022b. Prediction of oil content in single maize kernel based on hyperspectral imaging and attention convolution neural network. Food Chem. 395, 133563. https://doi.org/10.1016/j.foodchem.2022.133563.

Zhang, J., Guo, Z., Ren, Z., Wang, S., Yue, M., Zhang, S., Yin, X., Gong, K., Ma, C., 2023. Rapid determination of protein, starch and moisture content in wheat flour by near-infrared hyperspectral imaging. J. Food Compos. Anal. 117, 105134. https://doi.org/10.1016/j.jfca.2023.105134.

Zheng, H., Cheng, T., Li, D., Yao, X., Tian, Y., Cao, W., Zhu, Y., 2018. Combining unmanned aerial vehicle (UAV)-based multispectral imagery and ground-based hyperspectral data for plant nitrogen concentration estimation in rice. Front. Plant Sci. 9, 1–13. https://doi.org/10.3389/fpls.2018.00936.